

## 2 Design

### 2.1 High-fidelity Numerical Modelling of Spark Plug Erosion

---

Douglas Breden, Anand Karpatne, Kenta Suzuki, Laxminarayan Raja

#### Abstract

Spark plug erosion is critical in determining the overall efficiency of a spark ignition engine. Over its lifetime, a spark plug is subject to millions of firings. Each spark event results in material erosion due to several mechanisms such as melting, vaporization, sputtering and oxidation. With electrode wear, the inter-electrode spacing increases and a larger voltage difference is required to initiate the spark. The probability of engine misfires also increases with electrode erosion. Once a critical gap is reached, the energy in the ignition coil is not enough to cause a spark breakdown, and the spark plug must be replaced. Due to the long relevant time scales over which erosion occurs, and the difficulty of analyzing the spark plug environment during operation, determining spark plug lifetime typically requires extensive field testing. A high fidelity commercial thermal plasma solver, *VizSpark* is used simulate electrode erosion due to spark events. The model preserves key arc physics such as current conservation, conjugate heat transfer, fluid flow and electrode ablation. The solution framework includes the capability of coupling high fidelity arc physics with a dynamically deforming spark-plug electrode. A phenomenological model for electrode erosion based on energy is derived from prior experimental work on single-pulse electrode erosion. The energy based electrode erosion model is validated against experimental results, and 3-D electrode erosion simulations in stationary and cross-flow were performed.

#### 1 Introduction

The maximum lifetime of a spark plug is limited by electrode erosion. Over the course of 10's to 100's of millions of repeated sparking events, the electrode material ablates and the electrode gap increases. Eventually a point is reached where the spark-plug driving circuit is unable to provide the threshold voltage necessary to breakdown the gap and strike an arc. Essentially, the spark-plug is no longer operable and must be replaced. The issue of spark plug erosion has been investigated experimentally for many years now [1] [2] [3]. Spark plug erosion is a major issue in the long-term maintenance-free operation of a natural gas engine [4] [5]. Due to the long relevant time scales over which erosion occurs, and the difficulty of analyzing the spark plug environment during operation, determining spark plug lifetime typically requires extensive field testing.

The objective of this work is to develop a computational model that can accurately simulate the electrode erosion process and make predictions on the effective lifetime of a spark plug. The problem is challenging in that there are a vast range of time scales, all of which must be resolved to model the erosion. Time scales range from milliseconds needed to resolve arc physics up to weeks/months for timescales of electrode deformation due to ablation.

Previous numerical studies on spark igniters have focused predominantly on simulation of the arc itself [6] [7] [8] [9] [10] [11]. For predicting electrode erosion and lifetime, dynamic coupling between arc physics and an eroding electrode must be developed. In this study, a high-fidelity thermal arc solver is used to model the arc physics which determines the net heat and electrical energy fluxes to the electrodes. The solid electrodes themselves are modelled using an immersed object method, which allows for a dynamic change in shape of the electrode as the simulation progresses. Ablated mass flux from the electrodes is modelled using an energy dependent ablation model derived from experimental and numerical work performed by [1] [2]. As mass is removed from the electrode-gas interface, the immersed object dynamically deforms, which in turn modifies the gap voltage and the arc physics.

## 2 Model Description

Our general purpose commercial thermal plasma modeling solver *VizSpark*<sup>®</sup> [12] is used in this study. This high-fidelity computational tool has been utilized previously in the context of modeling arc formation, stretch and re-strike phenomena in a spark-plug gap [13] [14]. The physics represented in this tool involve solving compressible fluid flow physics coupled with the electromagnetic equations. The gas composition, thermal, electrical, and transport properties are solved by assuming chemical equilibrium. The thermal plasma model has been validated on a component basis to test the individual flow (viscous, inviscid), gas property thermodynamic and transport generation, and electromagnetic physics. Validation of the full arc physical has been performed for a spark channel in crossflow (see [14]) and for a stationary free-burning arc.

### *Arc Model*

Governing differential equations for the coupled fluid and electromagnetic physics are solved in a coupled manner.

### **Navier-Stokes Equations**

The compressible Navier-Stokes equations are solved to describe the mean-mass flow velocities, the gas pressure, mass density, and the arc (gas) temperature. The mass conservation equation can be written as

$$\frac{\partial \rho}{\partial t} + \vec{\nabla} \cdot (\rho \vec{V}) = 0 \quad (1)$$

where  $\rho$  is gas density, and  $\vec{V}$  denotes flow velocity. The momentum equation in conservative form can be expressed as

$$\frac{\partial(\rho \vec{V})}{\partial t} + \vec{\nabla} \cdot (\rho \vec{V} \vec{V}) = -\vec{\nabla} P + \vec{\nabla} \cdot \bar{\bar{\tau}} + \vec{S}_M \quad (2)$$

Here  $P$  denotes gas pressure,  $\bar{\bar{\tau}}$  corresponds to the viscous stress tensor and  $\vec{S}_M$  is the volumetric external force vector acting on the fluid. Finally, the energy equation can be written as

$$\frac{\partial(\rho E)}{\partial t} + \vec{\nabla} \cdot ((\rho E + P) \vec{V}) = (\bar{\bar{\tau}} \cdot \vec{\nabla}) \vec{V} + \vec{\nabla} \cdot (k \nabla T) + S_E \quad (3)$$

where  $E$  is specific internal energy (kinetic plus potential energy per unit volume of the fluid), ' $k$ ' corresponds to thermal conductivity and  $S_E$  is the external energy source. These governing equations are written in vector form as

$$\frac{\partial \vec{U}_{flow}}{\partial t} + \vec{V} \cdot (\vec{F}_{inv} + \vec{F}_{vis}) = \vec{S}_{flow} \quad (4)$$

Here, the vector of conserved variables  $\vec{U}_{flow}$  are listed below as

$$\vec{U}_{flow} = \begin{bmatrix} \rho \\ \rho u \\ \rho v \\ \rho E \end{bmatrix} \quad (5)$$

where ' $u$ ' and ' $v$ ' are the ' $x$ ' and ' $y$ ' components of velocity. The flow convective/inviscid flux  $\vec{F}_{inv}$  is given as

$$\vec{F}_{inv} = \begin{bmatrix} \rho u \\ \rho u^2 + P \\ \rho uv \\ (\rho E + P)u \end{bmatrix} \hat{x} + \begin{bmatrix} \rho v \\ \rho vu \\ \rho v^2 + P \\ (\rho E + P)v \end{bmatrix} \hat{y} \quad , \quad (6)$$

and the flow diffusive/viscous flux  $\vec{F}_{vis}$  is written as

$$\vec{F}_{vis} = \begin{bmatrix} 0 \\ \tau_{xx} \\ \tau_{xy} \\ u\tau_{xx} + v\tau_{xy} + k\frac{\partial T}{\partial x} \end{bmatrix} \hat{x} + \begin{bmatrix} 0 \\ \tau_{yx} \\ \tau_{yy} \\ u\tau_{yx} + v\tau_{yy} + k\frac{\partial T}{\partial y} \end{bmatrix} \hat{y} \quad (7)$$

Note that the energy diffusive flux consists of energy diffusion due to viscosity and heat conduction represented by Fourier's law. The viscous stresses can be found using the formula  $\tau_{x_j x_i} = \mu \left( \frac{\partial x_i}{\partial x_j} + \frac{\partial x_j}{\partial x_i} \right) + \lambda \delta_{ij} \vec{\nabla} \cdot \vec{V}$  where  $\mu$  is the coefficient of viscosity and  $\lambda$  is the bulk coefficient of viscosity. Stokes hypothesis is used to express the bulk viscosity term as  $\lambda = -\frac{2}{3}\mu$ . The last term in the coupled Navier-Stokes system of equations is the source term  $\vec{S}$  given as

$$\vec{S}_{flow} = \begin{bmatrix} 0 \\ (\vec{J} \times \vec{B})_x \\ (\vec{J} \times \vec{B})_y \\ \vec{J} \cdot \vec{E} - \dot{Q}_{rad} \end{bmatrix} \quad (8)$$

Here, Joule heating due to the electric field is modeled by the inclusion of  $\vec{J} \cdot \vec{E}$  source term on the fluid energy equation. Lorentz effects on the arc are modeled by including  $(\vec{J} \times \vec{B})$  forcing terms in the fluid momentum equations. The conduction current density

is  $\vec{J}$ , the electric field is  $\vec{E}$ , and  $\vec{B}$  is the local magnetic field. Cooling of the arc due to radiation is treated using a source term  $\dot{Q}_{rad}$  and a net emission coefficient model.

### Electromagnetic Equations

The governing equation to solve is the current continuity equation

$$\nabla \cdot \vec{J} = \dot{Q}_{rad} \quad (9)$$

Where the current density  $\vec{J}$ , is expressed using Ohm's Law

$$\vec{J} = \sigma(T, P) \vec{E} \quad (10)$$

Assuming that  $\vec{A}$  is the magnetic vector potential, such that  $\vec{B} = \nabla \times \vec{A}$ , the expression for

the electric field  $\vec{E}$  is modified to account for magnetic fields

$$\vec{E} = -\nabla\phi - \frac{\partial \vec{A}}{\partial t} \quad (11)$$

Equations (9), (10) and (11) in turn lead to the governing equation in the form of a second-order elliptic equation for electrostatic potential  $\phi$

$$\nabla \cdot \sigma \nabla \phi = 0 \quad (12)$$

For magnetic vector potential, the following time evolution equation is solved

$$\sigma \frac{\partial \vec{A}}{\partial t} + \sigma \nabla \phi - \frac{1}{\mu} \nabla^2 \vec{A} - \nabla \left( \frac{1}{\mu} \right) \times \nabla \times \vec{A} = 0 \quad (13)$$

### Immersed Boundary for Electrodes

Electrode (cathode) motion is accounted for by modeling the solid electrodes using an immersed boundary formulation [15]. The same governing equations for fluid flow and electric field are solved in the gas region and in the parts of the mesh that are tracked as immersed boundary electrodes.

The presence of the solid material is imposed by applying large numerical forcing terms on the 'x' and 'y'-momentum equations, essentially forcing the fluid velocity in the immersed object regions to zero [16]. Material properties of the solid are imposed in the regions of the immersed anode and cathode.

Removal and deformation of electrode surface cells is done by tracking the electrode mass in each cell, set at the start of the simulation using the material density and the cell volume. As ablation occurs at electrode-gas interfaces, tracked solid material mass is removed from the electrode and converted into vapor mass in the gas region. Once most of a cell's mass has been removed in this manner, the immersed object cell is converted into a gas cell indicating that it has ablated away. The new gas cell properties and variables are set using a cell clearing method (see [15]) where variables from neighboring gas cells are used to interpolate the newly cleared cell variables.

### Governing Equations in Immersed Electrodes

In the immersed electrode regions, the Navier-Stokes equations are modified with the addition of forcing terms that act to force the fluid velocity in the gas to go to zero. For the case of zero velocity, one can effectively ignore the x and y-direction momentum equations.

Diffusive heat transfer within the immersed objects and between the gas-solid interface is accounted for by the energy equation of the Navier-Stokes equations. The fifth row corresponding to the energy equation in the Navier-Stokes system reduces to the unsteady heat transfer equation

$$\frac{\partial \rho C_p}{\partial t} + \vec{\nabla} \cdot (\kappa \vec{\nabla} T) = 0 \quad (14)$$

To correctly model heat transfer within the immersed object, the effective density, thermal conductivity and specific heat of the immersed object cells are overridden with those of the metal being modeled (in this study copper is used).

For obtaining the electric fields, no modification to the governing equation for current continuity is necessary. The only requirement is to set the electrical conductivity of the immersed object electrodes to that of the electrode metal. Consequently, electric current can flow seamlessly through the electrodes, through the electrode-gas interface, and through the arc channel.

### Gas Properties

Closure of the governing equations requires specification of gas thermodynamic properties: the density and specific heats of the mixture; as well as transport properties: viscosity, thermal conductivity, and electrical conductivity. The approach with this model is to solve for all properties as a function of temperature and pressure and store the results in lookup tables.

Air thermodynamic and transport properties were obtained by assuming thermal and chemical equilibrium and applying Gibb's free energy minimization. First, the specific heats of the individual constituent species of air (NASA polynomials were used in this study), were provided as inputs. By solving Gibb's Free energy minimization problem, the species compositions as a function of temperature and pressure are obtained. Once the mixture composition is known, the mixture thermodynamic and transport properties can also be computed.

### Radiation Model

Arc radiation cooling is modeled using a net emission coefficient model, which acts as a cooling volumetric source term. Net emission coefficients are tabulated as a function of temperature and assumed to vary linearly with pressure. The net emission coefficient data for air was taken from [17].

### Energy Dependent Erosion Model

The mechanism of mass removal of material from a metal electrode surface is due to a multitude of complex physical phenomena that are not completely understood. Spark erosion occurs at length scales on the order of the arc root (tens of microns) and timescales of the order of nanoseconds to microseconds. Attempting to model all the

physical phenomena that can occur at the arc root such as sputtering, melting, vaporization, mass ejection, surface Joule heating and oxidation simultaneously with a simulation on the time and length scales required to resolve the spark is numerically infeasible. Therefore, developing a model that can accurately capture ablation yet avoid the numerical cost of modeling the arc root erosion process at full fidelity is imperative. Three mechanisms that have been investigated include sputtering of the surface due to ion bombardment, ejection of molten material due to an imbalance in the surface tension of the melt pool and an ion pressure force from the arc, and melting and vaporization of the material due to heat addition from the arc. The authors of [1] performed an experimental study of single spark ablation in an attempt to understand which of the proposed mechanisms (sputtering, melting/vaporization, or mass ejection) is the dominant ablation mechanism. They found that material ablation was strongly correlated to the energy required to melt the material. Furthermore, the ratio of ablated volume to input energy ( $V/E$ ) to the inverse of melting enthalpy (energy input required to melt the material per unit mass)  $\Delta H_{melt}$  for different pure metals (platinum, iridium, nickel, gold, silver, aluminum, nickel, tungsten, tin, lead, ruthenium, and copper) was calculated and plotted for pure air and nitrogen. The ratio or constant, herein referred to as the K-factor was found to be relatively close for all the pure metals [1].

$$K = \frac{V/E_{input}}{1/\Delta H_{melt}} \quad (15)$$

From the insights provided by the experimental and numerical work in [1] [18] [19], a phenomenological model for mass flux from a surface due to an input energy has been determined. Using the K-factor defined above, the erosion mass flux rate  $\vec{\Gamma}_{eroded}$  at a surface can be modelled as

$$\vec{\Gamma}_{eroded} = K \frac{\rho \dot{E}_{input}}{\Delta H_{melt}} \quad (16)$$

$\dot{E}_{input}$  is an input power flux ( $W/m^2 \cdot s$ ),  $\rho$  is the density of the bulk metal, and  $\Delta H_{melt}$  is the energy per kg mass required to melt the material from a reference temperature. What this equation essentially says is that erosion is strongly correlated to the input energy, the amount of mass (density) that can absorb the energy, and the energy required to melt that mass. The K-factor is relatively insensitive to the material type and accounts for the detailed physics such as radiation, surface Joule heating/ that this model tries to abstract away.

The chief advantage of this model is its simplicity: the surface ablation which involves complex interaction between the arc root and the metal is simplified to a function of three material dependent constants (K,  $\Delta H_{melt}$ , and  $\rho$ ) and an input energy. The input power for the model at the surface can either be electrical energy (the surface voltage times the surface current) or the net incident heat flux, both of which are obtainable from an arc solver.

### 3 Arc Root Scale Erosion Modelling

The energy dependent erosion model utilized in this study depends on obtaining the material dependent K-factor. The input energy can be specified as either the electrical or incident heat flux energy. This factor can be calculated either from experiments [18] or through high-fidelity thermal modeling near the arc root [19]. The amount of eroded

volume is correlated with the amount of melt pool for a given arc energy and electrode material. In this section, an estimate of the melting and heating of the arc spot for a given input energy at the arc time scale is performed. Note that the current study is an essential first step in numerically determining K-factor. The eventual goal is to develop a computational tool can be used to perform high fidelity modelling of the heating and melting of the metal surface near the arc root to obtain the K-factors. Once K-factors are known, the same computational tool can be used to simulate the full spark-plug erosion problem. This work is similar to and mostly follows that done in the simulation work of [19].

The same domain and input energy profiles from [19] are used here. A key requirement is the ability to predict material erosion is to track the material phase transition. One approach is to explicitly track the phase of the material using a phase variable as was done in [19]. In this work, instead of explicitly tracking the material phase, the material properties of the metal across all phases over a range of temperatures are tabulated and the phase change is accounted for in the specification of the material's temperature dependent thermodynamic and transport properties. The energy required to change phase (latent heat of fusion for solid to liquid and latent heat of vaporization for liquid to gas) is accounted for in the specification of the specific heat of the material.

### Solid Material Properties and Phases

Temperature dependent material properties are specified for each metal. Thermodynamic properties include temperature dependent density and specific heat and the transport properties include temperature dependent thermal conductivity. A sample of the thermodynamic and transport properties for nickel over a temperature ranging from 1000 K to 4000 K are shown in Figure 1.

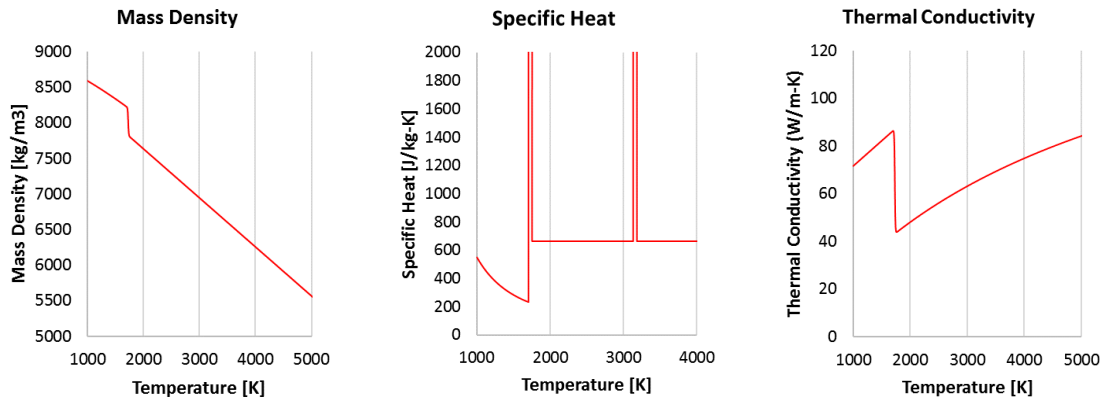


*Figure 1: Temperature dependent thermodynamic and transport properties for nickel. The energy of phase transition is accounted for in the material specific heat*

The phase change of the material is accounted for by modifying the specific heat with the energy required to undergo the phase change from the formula for the enthalpy of fusion/vaporization

$$\Delta H_{vap} = \int_{T_0}^{T_{melt}} C_p(T) dT + L_{fusion} + \int_{T_{melt}}^{T_{boil}} C_p(T) dT + L_{vaporization} + \int_{T_{boil}}^T C_p(T) dT \quad (17)$$

The total energy required to heat a material from a referenced temperature  $T_0$  to  $T$  is obtained by integrating the specific heat over the temperature range. When the temperature reaches the melting and boiling points of the material, the latent heat of fusion

and vaporization respectively, are added to account for energy required for the phase transformation.

The formula for enthalpy of fusion/vaporization can be used to derive a modified specific heat function. We assume that phase transformation occurs over a small but finite temperature interval  $\Delta T_{ph}$  (10 K) and that the heat of fusion/vaporization can be re-expressed as a constant specific heat times the finite interval temperature.

$$L_{fusion} = C_{p,fusion}\Delta T_{ph} \quad (18)$$

$$L_{vaporization} = C_{p,vaporization}\Delta T_{ph} \quad (19)$$

Hence the total energy required to undergo phase change from solid, to liquid, to gas is conserved and can be expressed purely as a function of a piecewise continuous specific heat function

$$\Delta H_{vap} = \int_{T_0}^{T_{melt}} C_p(T)dT + C_{p,fusion}\Delta T_{ph} + \int_{T_{melt}}^{T_{boil}} C_p(T)dT + C_{p,vaporization}\Delta T_{ph} + \int_{T_{boil}}^T C_p(T)dT \quad (20)$$

### Simulation Configuration

A two-dimensional 40 x 40 micron axisymmetric quad mesh is used for all simulations.

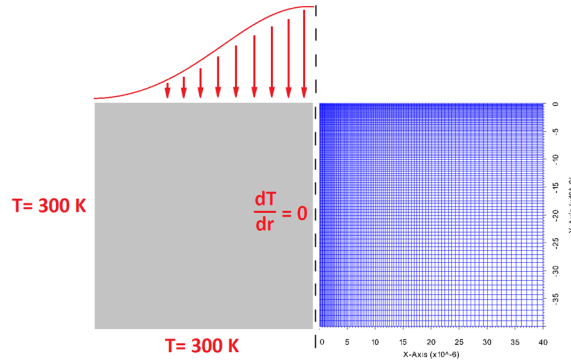
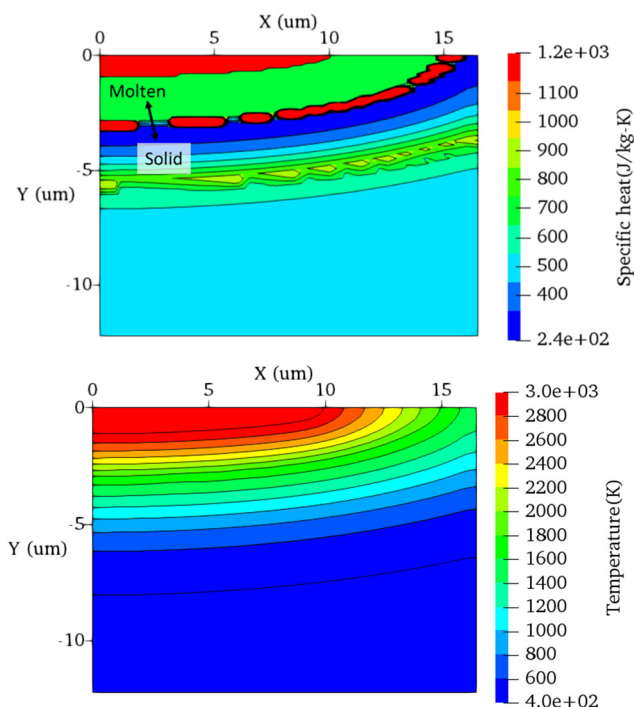


Figure 2: Axisymmetric configuration with boundary conditions (left) and numerical mesh (right)

Fixed temperature boundary conditions are applied at the bottom and side, and a zero-temperature gradient boundary condition is applied along the axis. For comparison with [19], the same energy deposition profile (gaussian in space and gaussian in time) was chosen, as shown in Figure 2. A quad mesh with a size of 0.1 micron was chosen (close to the axis boundary).

## Results

Simulations were completed for the following metals: tungsten (W), iridium (Ir), nickel (Ni), platinum (Pt), copper (Cu), gold (Ag), and aluminum (Al). The specific heat and temperature profiles for nickel at the end of 1 microsecond are shown in Figure 3. The specific heat profile spikes at phase transitions due to the addition of the latent heat of fusion and vaporization, and acts as an indirect marker of the location of phase transition. For nickel, the phase transition region along the region where specific heat spiked (undergoing phase transition) from solid to molten nickel is indicated at the top of Figure 3. The temperature of the nickel melt pool reaches a peak of approximately 3000 K with a depth of approximately 3 microns. The melt pool radius is about 15 microns compared to the imposed arc root radius (radius where heat was applied) of 10 microns.



*Figure 3: Specific heat (top) and temperature (bottom) profiles for nickel after 1 millisecond of simulation time. The solid-molten transition region can be identified by the large spike in specific heat and is indicated with arrows.*

Figure 4 shows a comparison between melt pool volume prediction from the arc solver and numerical results from Lasagni et al. [19] for different ratios of eroded volume to spark energy. The data points correspond to different materials. It can be observed that the molten pool volume prediction from the arc modelling tool agrees well with previous results from [19].

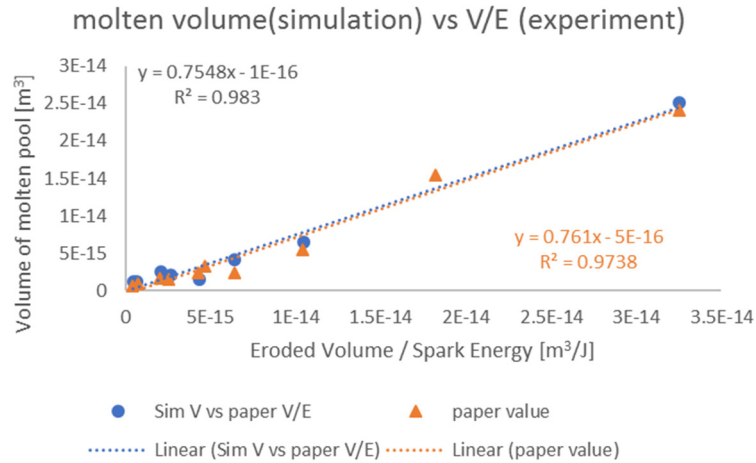


Figure 4: Comparison of volume of molten volume pool vs V/E of current simulations with simulations of [19].

The molten pool volume prediction is only the first step in determining the K-factor. Materials with larger molten pool volume are susceptible to more erosion due to vaporization, oxidation, and ejection of melt pool volume due to an imbalance of surface tension forces on the electrode surface. Therefore, Figure 4 can be used to quantify erosion trends for different materials. More work is necessary to accurately determine eroded volume for every electrode material/spark energy combination. Therefore, for the rest of this study, the electrical energy dependent K-factor based on previous experimental data [2] is used.

## 4 Validation of Energy Dependent Erosion Model

Given an energy dependent K-factor for electrode erosion, the above described model is validated against prior experiments [2] [1] for tungsten (W), iridium (Ir), nickel (Ni), platinum (Pt), tin (Sn) and silver (Ag). The inputs to the model are geometry, electrical parameters and the predicted outputs are volume of eroded electrode and the total spark discharge energy. The surface electrical energy dependent K-factor for air are taken from [1].

### Simulation Configuration

The geometry (Figure 5) consists of an axisymmetric pin-to-plane spark plug, with a cylindrical cathode (diameter 1 mm), and a conical anode (max diameter 0.6 mm). The mesh consists of variable sized triangles across the entire domain. At the cathode boundary, a fixed current profile is applied (Figure 6) with a peak amplitude of 0.9 A that decreases linearly to 0 over 1.1 milliseconds. The anode boundary is treated as electrically grounded. For the outer boundaries, a symmetry condition is applied such that there are no far-field gradients in flow or electric field variables.

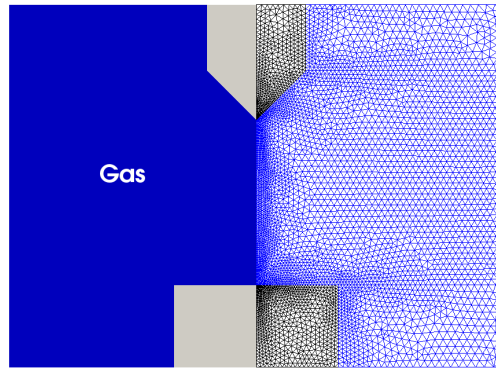


Figure 5: Domain and mesh for the pin to plane arc simulation. The mesh consists of 9,664 cells. The anode (top electrode) is conical in shape with base diameter of 0.6 mm, and the cathode (bottom electrode) is cylindrical (diameter 1 mm).

Figure 6 shows the applied cathode current as a function of time and the predicted boundary voltages. Initially, as a large current is applied, the cathode voltage increases self-consistently to allow for the passage of current. This high voltage ( $\sim 1000$  V) causes significant local joule heating and an arc channel forms with increased conductivity. Once this channel is established, the cathode potential drops down to  $\sim 50$  V. Finally, when the applied current approaches zero (after  $\sim 1$  ms), the cathode voltage again increases due to a drop in the channel temperature and conductivity. Finally, when the applied current drops down to zero, the electrode voltage also reduces to zero as no current flows between the spark-gap.

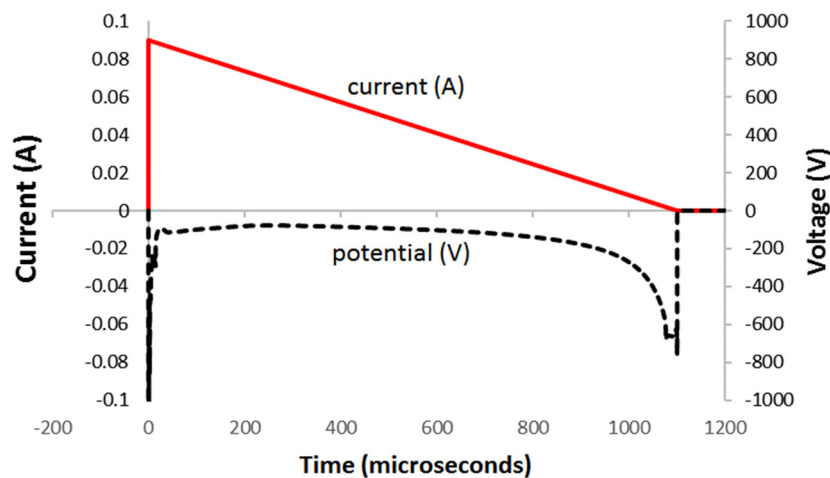


Figure 6: Current and Voltage as function of time for the pin-plane simulation using platinum as the cathode material. Current is the applied (input) boundary condition and the voltage is obtained by the arc solver self-consistently.

The volumetric current density and temperature snapshots are shown in Figure 7. Initially, when the arc forms (0.05 milliseconds), the current density is maximum ( $\sim 10^8$  A/m<sup>2</sup>) and concentrated along the axis. The arc temperature is also maximum along the centerline ( $\sim 6000$  K). With time, as the total applied current diminishes, the current density magnitude reduces to  $\sim 10^6$  A/m<sup>2</sup>.

## 2.1 High-fidelity Numerical Modelling of Spark Plug Erosion

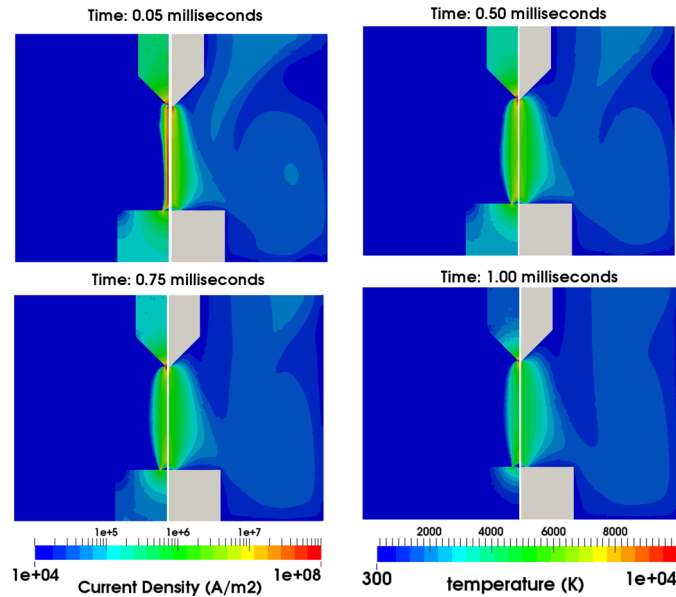


Figure 7: Time snapshots of the current density (left half) vs temperature (right half) in the arc channel for 0.25, 0.5, 0.75 and 1 milliseconds. Note that the current density through the metal electrodes is also included.

The comparison between experiments and predicted results is shown in Figure 8. The x-axis corresponds to the inverse of material melting enthalpy (varies with material type), and the y-axis denotes the ratio of volume eroded to input spark energy. The spark energy is obtained by integrating cathode electrical power (product of electrode voltage and current from Figure 6) over the entire spark duration. Given an instantaneous electrical power, eroded volume flux is computed using Eq. 16. Finally, the ratio of total eroded volume to spark energy is obtained for different material types. Good correlation with experimental data is observed, and all data points lie along a straight line with a slope of  $K = 2.095811 \times 10^{-5}$ .

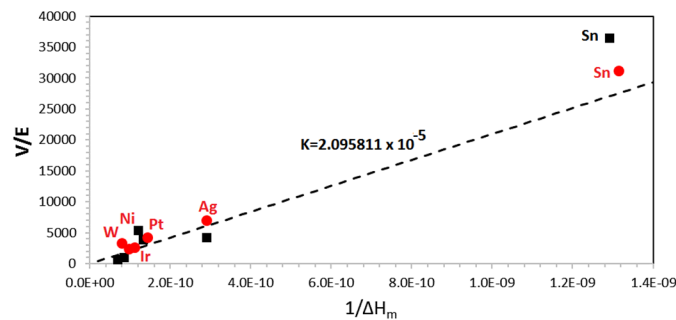


Figure 8: Comparison of calculated eroded volume/energy vs the reciprocal of material melting enthalpy ( $1/\Delta H_m$ ) from simulations (red circles) to experimental values (black squares) from [1].

## 5 3-D Spark Plug Erosion Prediction

Spark erosion occurs over many millions of spark events. Simulating millions of sparking events at high fidelity is numerically infeasible with current computing power. We utilize several approximations and techniques to approximately capture the erosion

that occurs over long time scales and millions of firings with only a few high-fidelity simulations.

A typical spark duration for a car ignition system is of the order of 1 millisecond and for inductive ignition systems the current profile will often have a sawtooth waveform [13]. In this work the electrical input boundary condition is specified as a sequence of sawtooth current wave form pulses with an initial peak of 50 mA which then decrease linearly to zero (see Figure 11 and Figure 14).

The rate at which ablation takes place along the electrode surface can be accelerated beyond the timescale of the arc event by applying a multiplicative factor to the surface erosion rate calculated by the surface erosion model. For example, if a single spark event is simulated and an erosion rate multiplier of 100,000 is used, that single sparking event would remove roughly the equivalent mass to 100,000 spark events.

Another acceleration technique used to reduce simulation time is to use shorter pulses in tandem with the surface erosion rate multiplicative factor. Because the erosion model is energy dependent, a multiplicative factor on the input energy can be used to approximate energy input from a longer pulse.

### Simulation Configuration

A 3-D domain for the sparkplug consisting of a prong cathode and an L-jacket grounded anode similar to the spark plug geometry from [13] is specified and shown in Figure 9. Two ablation prediction simulations are performed: one with an air cross-flow of 8 m/s and another in stationary air. The pressure is 5 bar and the ambient temperature at the start of simulation is 300 K. For the case with 8 m/s cross-flow, the inflow direction is indicated in Figure 9 and the other boundaries are outflow/far-field boundaries. An electrical current is specified on the cathode bottom boundary as a function of time and a zero voltage (grounded) boundary condition is specified for the anode L-jacket.

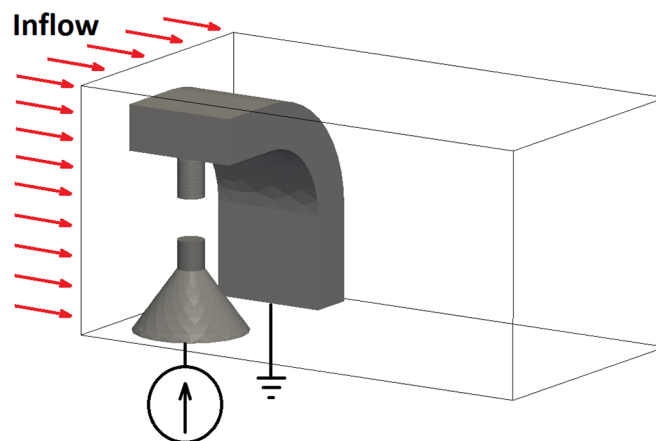


*Figure 9: Domain for 3-D sparkplug with constant current power source and grounded L-jacket. The boundary where inflow is applied is shown with red arrows.*

A numerical mesh consisting of 328,287 tetrahedral cells is imposed on the problem domain and shown in Figure 10. A domain decomposition approach is utilized, where

the numerical mesh is split equally amongst multiple processors and solved in parallel to reduce the computational solve time.

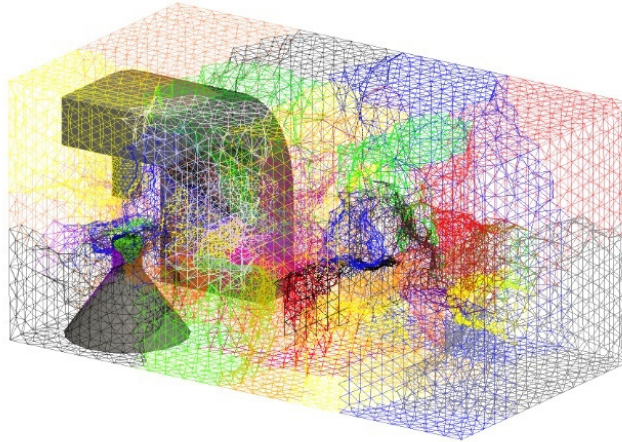


*Figure 10: The numerical mesh consisting of 328,287 cells split amongst 40 computing processors.*

For both flow and no-flow simulations, 10 numerical pulses of 0.1 milliseconds are applied. Each pulse consists of applying an input current with peak current of 50 mA which then decreases linearly to zero (sawtooth pulsing).

In this work, the simulated pulses are 0.1 milliseconds in duration with an input energy multiplier of 10 such that the effective pulse duration is 1 millisecond. In addition to pulse energy multiplier, we apply an erosion multiplicative factor of 100,000 such that each simulated pulse removes the mass that approximately 100,000 real pulses would remove.

Each simulated pulse is separated by 20 microseconds of zero-current off time. During the pulse off-time, an artificially large energy source term is applied to quench the arc temperature channel such that each simulated pulse is applied to fresh gas and ensuring that each simulated spark is independent of the prior simulated arc.

The cross-flow and no cross-flow simulations were each simulated using parallel domain decomposition on 40 processors. The total run time required to complete each simulation is approximately 3-4 days.

## Results

### *Cross-Flow (8 m/s):*

The results for the simulation with an 8 m/s cross-flow are presented first. Figure 11 presents time snapshots of the arc temperature and the electrode surface topology at the end of each simulated pulse. One can see the arc stretch due to the cross-flow in each of the images and the steady removal of cells on the powered cathode as the simulation evolves with time.

## 2.1 High-fidelity Numerical Modelling of Spark Plug Erosion

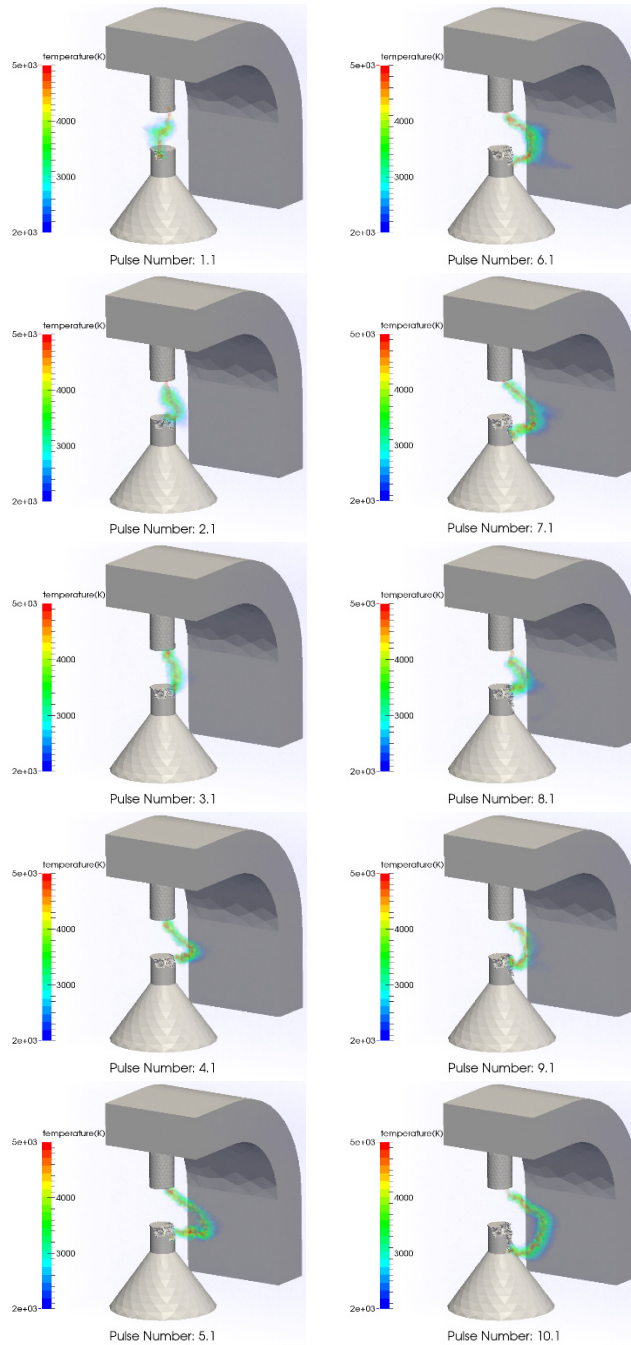


*Figure 11: Time transients of the arc channel and electrodes for the sparkplug in 8 m/s crossflow at start of each simulated pulse (10 pulses total).*

Figure 12 presents the current applied and voltage measured at the base (bottom side) of the powered electrode as function of pulse. The current was applied in a series of saw-tooth pulses and the voltage on the electrode is obtained self-consistently by the solver. Note the initially high voltage spike at the start of each current pulse indicating gas breakdown. Note also, the increase in voltage as the arc stretches with the cross-flow.

## 2.1 High-fidelity Numerical Modelling of Spark Plug Erosion

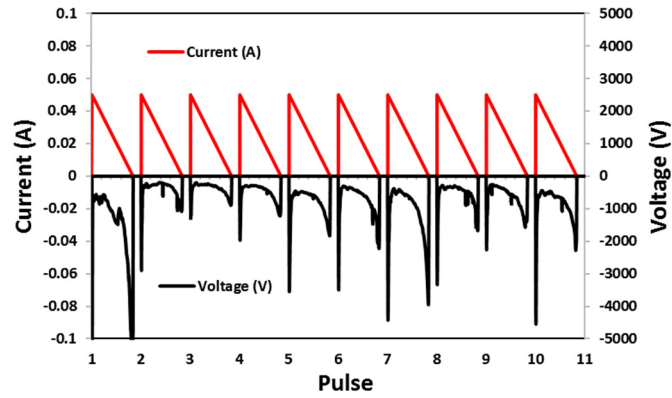
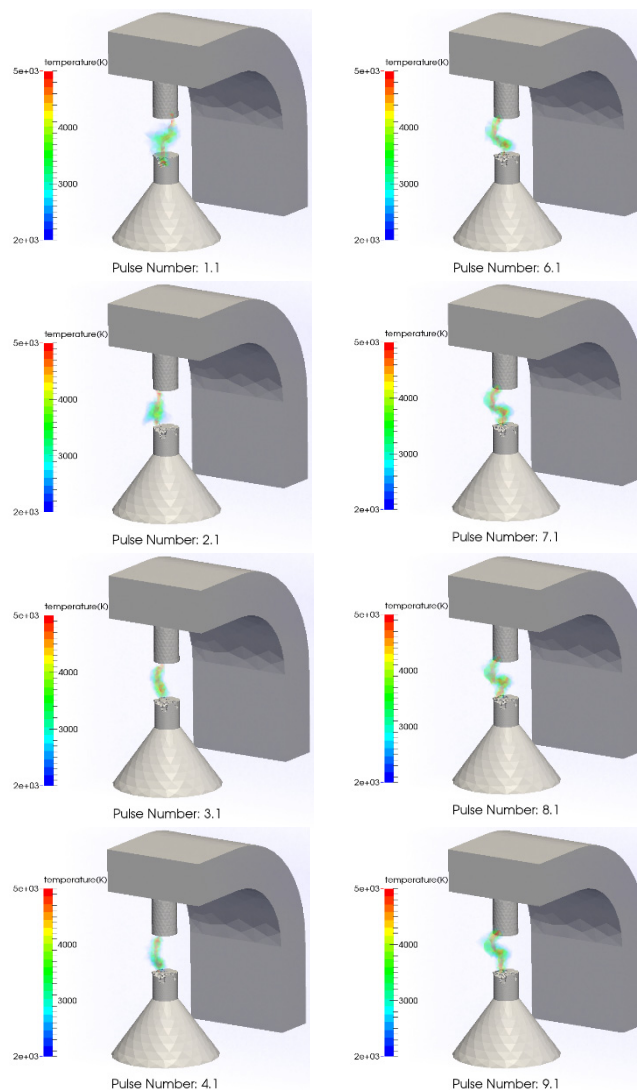


Figure 12: Electric current (top) and voltage (bottom) transients as function of applied pulse for the simulation with cross-flow.

*Stationary (No Cross-Flow):*

The same simulation configuration is repeated with no-crossflow to determine the impact of flow on spark life time.



## 2.1 High-fidelity Numerical Modelling of Spark Plug Erosion

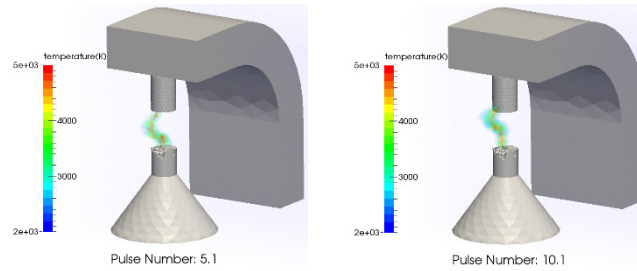


Figure 13: Time transients of the arc channel and electrodes for the sparkplug in stationary flow at start of each simulated pulse (10 pulses total).

The voltage and current transients as a function of individual pulses are shown in Figure 14. The same saw-tooth current profile that was used for the cross-flow case is used as a boundary condition input to the cathode. The voltage profile displays voltage peaks during breakdown and a slow increase in the voltage. Compared to the case with cross-flow (Figure 12), the peak voltages are lower and the magnitude of voltage increase over each pulse duration is lower. The lower voltages indicate that the spark channel resistance in the no-flow case is lower compared to the cross-flow case. This makes sense intuitively as the channel length and hence channel resistance is lower when there is now cross-flow compared to the case when there is cross-flow and arc stretch.

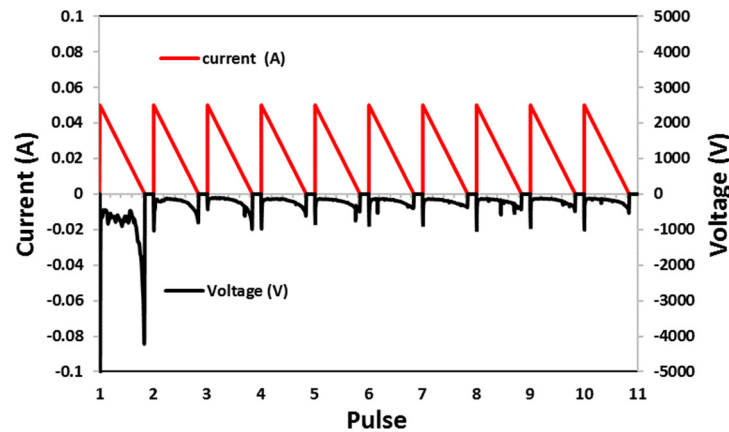
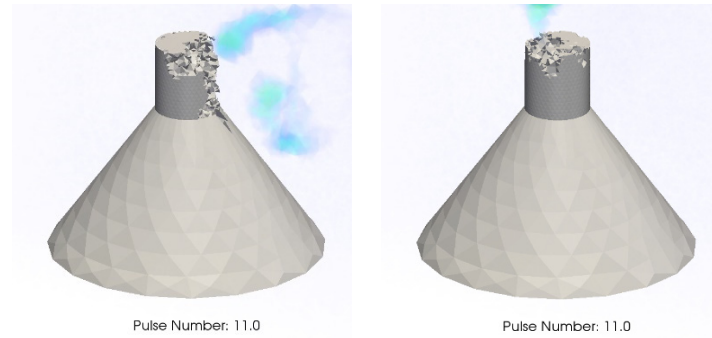


Figure 14: Electric current (top) and voltage (bottom) transients as function of applied pulse for the simulation with no cross-flow.

The erosion profile of the powered electrode (cathode) for the case with and without cross-flow are compared in Figure 15. The cross-flow case shows preferential wear on the downwind side of the electrode.



*Figure 15: Erosion profiles for sparkplug cathode after 10 simulated pulses for the case with 8 m/s crossflow (left) and case with no cross-flow (right).*

The eroded mass of the powered electrode (cathode) for 8 m/s cross-flow and stationary flow compared in Figure 16. Two trends are noticeable: the first is that during breakdown at the start of each pulse there is more mass removal then during the arc phase. The second is that the net eroded mass is higher for the case of cross-flow. The observation that increased material erosion is observed for the case of cross-flow can be explained through the following argument. The supplied current for both simulations is the same yet cross-flow stretches the arc. The arc channel can be thought of as a resistive element, hence a longer stretched arc will have more electrical resistance than a non-stretched arc. More energy is required to maintain a stretched arc compared to a stationary arc and because electrode erosion is a function of electrical energy deposition, more energy will also go into the electrodes which leads to more erosion.

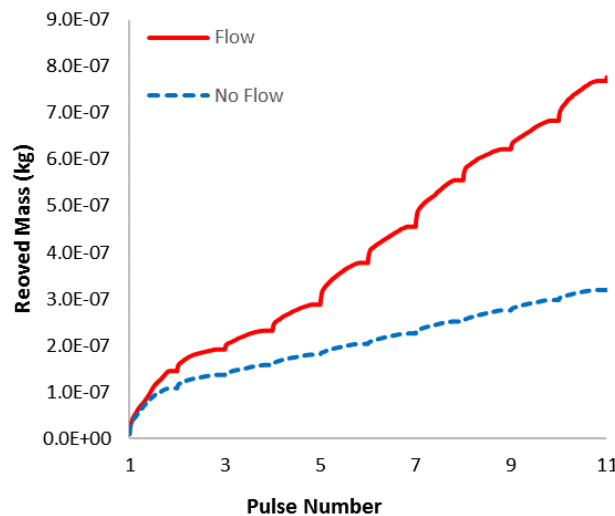


*Figure 16: Eroded electrode (cathode) mass as a function of simulated pulses. The eroded mass for stationary flow is shown with the dashed line (blue). Eroded mass for the cross-flow case is shown with the solid line (red).*

## 6 Summary and Conclusions

In summary, a roadmap for simulating erosion of spark plug electrodes has been presented. Based on experimental studies of single spark electrode erosion, an energy dependent phenomenological model for electrode erosion based on the strong correlation between input energy and the energy required to melt the material is formulated.

The energy dependent model for electrode erosion is validated by comparing single-pulse simulated electrode erosion rates with experimentally determined erosion rates. Using the energy dependent erosion model, simulations of electrode erosion from a sample spark plug were performed for stationary and cross-flow configurations. It was found that cross-flow induced arc stretch increases the arc resistivity and hence the energy deposition into the arc channel and the electrodes. This resulted in an increased net electrode erosion for cross-flow compared to no cross-flow when input current was the same for the two cases.

## References

- [1] F. A. Soldera, F. T. Mucklich, K. Hrastnik and T. Kaiser, "Description of the discharge process in spark plugs and its correlation with the electrode erosion patterns," *IEEE Transaction on Vehicular Technology*, vol. 53, no. 4, 2004.
- [2] A. Lasagni, F. Soldera and F. Mucklich, "Quantitative investigation of material erosion caused by high-pressure discharges in air and nitrogen," *Zeitschrift für Metallkunde*, vol. 95, no. 2, pp. 102-108.
- [3] R. Maly, "Spark ignition: its physics and effect on the internal combustion engine," in *Fuel Economy*, 1984, pp. 91-148.
- [4] H. Lin, M. P. Brady, R. K. Richards and D. M. Layton, "Characterization of erosion and failure processes of spark plugs after field service in natural gas engines," *Wear*, vol. 259, pp. 1063-1067, 2005.
- [5] S. Javan, S. V. Housseini, S. S. Alaviyoun and F. Ommi, "Effect of electrode erosion on the required ignition voltage of spark plug in CNG spark ignition engine," *The Journal of Engine Research*, vol. 26, pp. 31-39, 2012.
- [6] M. Akram and E. Lundgren, "The evolution of spark discharges in gases: I. Macroscopic models," *J. Phys. D: Appl. Phys.*, vol. 29, pp. 2129-2136, 1996.
- [7] M. Arkam, "The evolution of spark discharges in gases: II. Numerical solution of one-dimensional models," *J. Phys. D: Appl. Phys.*, vol. 29, pp. 2137-2147, 1996.
- [8] R. Reinmann and M. Akram, "Temporal investigation of a fast spark discharge in chemically inert gases," *J. Phys. D: Appl. Phys.*, vol. 30, pp. 1125-1134, 1997.
- [9] M. Thiele, S. Selle, U. Riedel, J. Warnatz, R. Schießl and U. Maas, "A detailed two-dimensional numerical study of spark ignition including ionization," *SAE Technical Paper*, 2002-01-1110.
- [10] R. Dahms, T. D. Fansler, M. C. Drake, T. W. Kuo, A. M. Lippert and N. Peters, "Modeling ignition phenomena in spray-guided spark-ignited engines," *Proceedings of the Combustion Institute*, vol. 32, pp. 2743-2750, 2009.
- [11] O. Ekici, O. A. Ezekoye, M. J. Hall and R. D. Matthews, "Thermal and flow fields modelig of fast spark discharges in air," *Journal of Fluids Engineering*, vol. 129, no. 55, 2007.
- [12] VizSpark Manual, Esgee Technologies, 2016.

- [13] T. Shiraishi, A. Teraji and Y. Moriyoshi, "The Effects of Ignition Environment and Discharge Waveform Characteristics on Spark Channel Formation and Relationship between the Discharge Parameters and the EGR Combustion Limit," *SAE International*, 2015.
- [14] D. Breden, A. Karpatne and L. Raja, "Modelling of Electrode Erosion for Prediction of Spark Plug Lifetime," in *WCX World Congress Experience* , Detroit, 2018.
- [15] R. Mittal and G. Iaccarino, "Immersed Boundary Methods," *Annu. Rev. Fluid Mechanics*, vol. 37, pp. 239-61, 2005.
- [16] S. Patnakar, Numerical Heat Transfer and Fluid Flow, New York: Mcgraw-Hill, 1980.
- [17] T. Billoux, T. Cressault, P. Teulet and A. Gleizes, "Calculation of the net emission coefficient of an air thermal plasma at very high pressure," *Journal of Physics: Conference Series*, vol. 406, 2012.
- [18] F. Soldera, A. Lasagni, F. Mucklich, T. Kaiser and K. Hrastnik, "Determination of the Cathode Erosion and Temperature for the High Voltage Discharges using FEM Simulations," *Computational Materials Science*, vol. 32, pp. 123-139, 2005.
- [19] A. Lasagni, F. Soldera and F. Mucklich, "FEM Simulation of Local Heating and Melting During Electrical Discharge Plasma Impact," *Modelling Simul. Mater. Sci. Eng.*, vol. 12, pp. 835-844, 2004.